ACS APPLIED MATERIALS & INTERFACES

Letter

www.acsami.org

Hollow Ball-in-Ball $Co_xFe_{3-x}O_4$ Nanostructures: High-Performance Anode Materials for Lithium-Ion Battery

Lisha Shen,[†] Huawei Song,[†] Gongzheng Yang,[†] and Chengxin Wang*[,†,‡]

[†]State Key Laboratory of Optoelectronic Materials and Technologies, School of Physics Science and Engineering, and [‡]The Key Laboratory of Low-Carbon Chemistry & Energy Conservation of Guangdong Province, Sun Yat-sen (Zhongshan) University, Guangzhou 510275, People's Republic of China

Supporting Information

ABSTRACT: The intrinsic electronic conductivity can be improved by doping efficiently. $Co_xFe_{3-x}O_4$ nanostructures have been synthesized for the first time to improve the conductivity of lithium battery electrode. The solid solution $Co_xFe_{3-x}O_4$ were characterized by X-ray diffraction pattern (XRD), Raman spectrum, scanning electron microscopy (SEM), transmission electron microscope (TEM), electrochemical impedance spectroscopy (EIS), and cyclic voltammetry (CV). The results show that the doping enlarge the lattice spacing but the structure of Co_3O_4 is stable in the Li-ion intercalation/deintercalation process. The AC impedance spectrum reveals the conductivity is well improved. In addition, the solid solution $Co_xFe_{3-x}O_4$ exhibit excellent electrochemical characteristics. The electrodes with 20% molar ratio of Fe ions own a reversible capacity of 650.2 mA h g^{-1} at a current density of 1 A g^{-1} after 100 cycles.

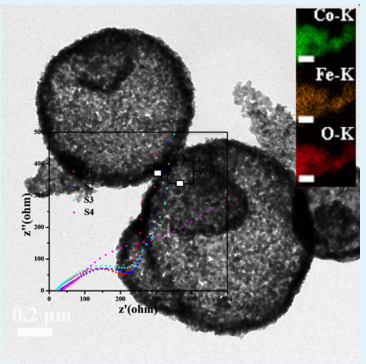

KEYWORDS: *ball-in-ball, solid solution, template-free, hydrothermal, lithium-ion battery*

INTRODUCTION

Transition metal oxides (TMOs) attract wide attention as promising candidates for next-generation anode materials.[1−4] They possess a unique lithium storage mechanism—conversion reaction ($MO_x + xLi^+ + xe^- \rightarrow M + xLi_2O$) and higher theoretical capacity (500−1000 mAh g^{-1}) than commercialized graphite (~372 mAh g^{-1}).[5,6] However, most TMOs usually suffer from the problem of poor conductivity and severe volume change in the process of Li^+ insertion/extraction, which will destroy the structure and result in rapid capacity loss especially at high charge−discharge rates.[7−10] To increase the electronic conductivity, researchers most commonly adopt electronically conductive materials (carbon, small metal particles, and conductive polymers) coatings.[11−17] Wang et al. synthesized C/Fe_3O_4 composite nanofibers by electrospinning, and the C/Fe_3O_4 composite nanofiber exhibits a high reversible capacity, good cycling performance, and excellent rate capability.[16] The carbon not only can enhance the conductivity but also accommodate the volume change upon Li^+ insertion and extraction.[7,10,18,19] In addition, doping alien cations is usually adoped to improve the intrinsic conductivity for cathode materials.[12,17,20−22] The impurity ionization will increase the electron density and improve the conductivity of acceptor. Liu et al. studied the effect of Zn-doping on the electrochemical performance of $LiFePO_4$.[17] The doping Zn increase the lattice spacing, which can accommodate more lithium ion. In the meantime, the charge transfer resistance is reduced and the cycling stability is well-improved. Matsumura et al. synthesized the α-Fe_2O_3−SnO_2 solid solution by a wet preparation method using a precipitation from alkaline solutions containing Fe^{3+}, Sn^{4+}, and SO_4^{2+} ions.[23] Xu and co-workers synthesized a two-demensional V_2O_5 and manganese-doped V_2O_5 sheet network by a one-step polymer-assisted chemical solution method.[24] The doped cell showed higher electrical conductivity, specific discharge capacity, and cycle life than the undoped cells.

In this paper, Fe-doped Co_3O_4 solid solution nanostructures were synthesized via a simple hydrothermal method and a post heat treatment. With similar radius and electronegativity, Fe and Co exhibit impressive lattice compatibility in their solid solutions.[25] Through pH-dependent hydrothermal processes, the morphology and solute amount are well controlled in the precursors. The precursors were annealed at 500 °C for 3 h to recrystallize and form the targeted hollow solid-solution nanocomposites. Benefiting from the hollow structure and the doping-related effects, the volume effect and pulverization are well-alleviated. Meanwhile, the conductivity is significantly improved. Consequently, stable cycling, excellent storage capability, and rate performance are simultaneously achieved in the solid solution.

RESULTS AND DISCUSSION

The ICP results of the samples are shown in Table 1, which indicate x = 2.40, 2.69, 2.88, and 3 for samples S1, S2, S3, and

Received: February 14, 2015
Accepted: May 15, 2015
Published: May 15, 2015

DOI: 10.1021/acsami.5b01452
ACS Appl. Mater. Interfaces 2015, 7, 11063−11068

Table 1. ICP Results of the Samples

sample	Fe (mg/L)	Co (mg/L)
S1	7.283	29.432
S2	1.369	11.993
S3	0.144	3.401
S4	≤0.215	0.965

S4, respectively. The morphology and size of solid solution were examined by SEM and TEM. Figure 1 shows the SEM and TEM (inset) imagines of precursors of S1, S2, S3, and S4. As shown in Figure 1a–d, there are no significant differences between bare and Fe-doped samples, unlike the noticeable change that effects electrochemical performance in other groups' results. All samples have spherical morphologies and diameters of about 1–2 μm. The microspheres are hollow ball-in-ball structure, certified by TEM images (Inset). Accordingly, the primary reason for enhancement of electrochemical performance caused by Fe doping in this report is not originated from the microscopic properties such as morphology and particle size. Figure S5 in the Supporting Information gives the energy disperse spectrum (EDS) analysis of S1, revealing the presence of Co, Fe, and O elements.

Figure 1e shows the XRD patterns of the undoped S4 and the doped S1, S2, and S3 products. The XRD pattern of undoped S4 is indexed to standard cubic Co_3O_4 (JCPDS No.43–1003). All the diffraction peaks of the doped samples have similar lattice parameters as those of cubic Co_3O_4 according to JCPDS No.43–1003. But the peaks of the doped shift from the undoped one. The lattice structure of Co_3O_4 is stable because of the low doping concentration of Fe ion and the almost similar ion radius of Fe^{2+} and Co^{2+}. Furthermore, with the content of Fe ion increasing, the deviation gets stronger, indicating that the d values were gradually increased by Fe^{2+} doping. The doped Fe results in the expansion of the lattice of the solid solution due to the large atomic radii of the dopant of Fe. The expansion in lattice crystal could provide more space for lithium intercalation/deintercalation.[12,17]

Figure S1a in the Supporting Information shows the Raman spectra of the Co_3O_4 and solid-solution $Co_xFe_{3-x}O_4$, which

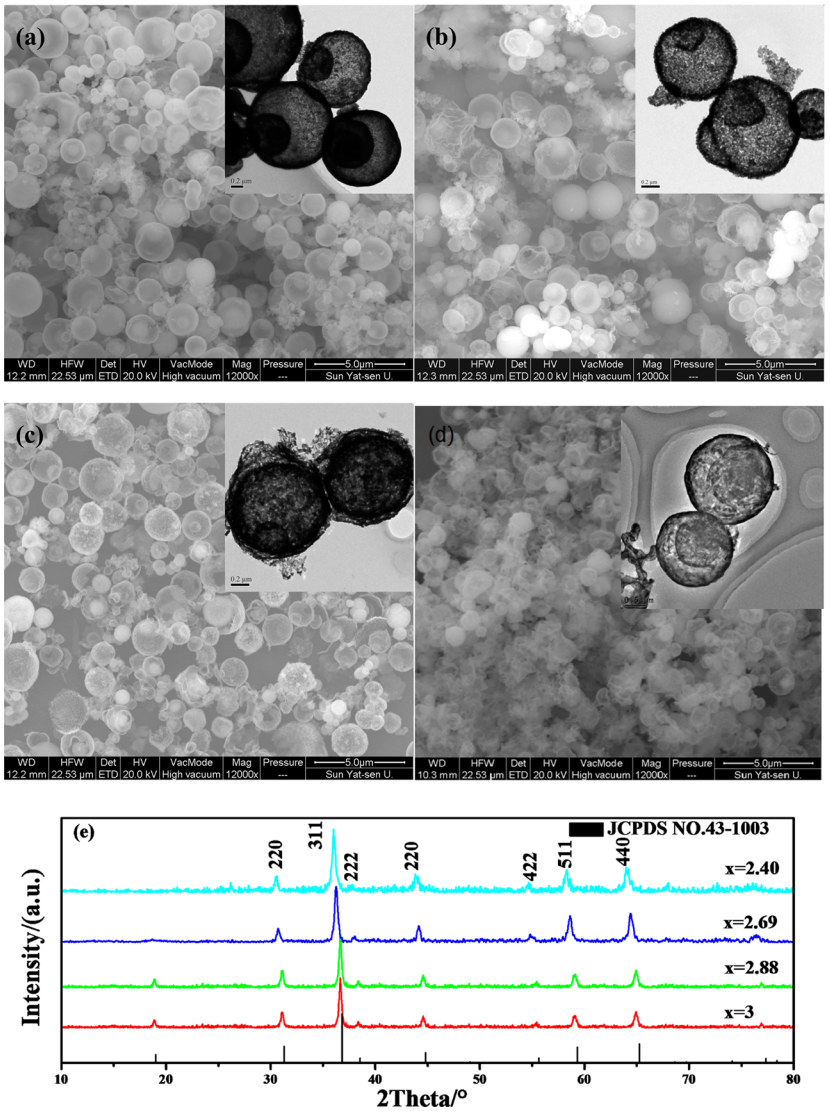

Figure 1. (a–d) Morphology and microstructure of the solid solution $Co_xFe_{3-x}O_4$: SEM and TEM (inset) mages for S1, S2, S3, and S4. (e) XRD patterns of the solid-solution $Co_xFe_{3-x}O_4$.

DOI: 10.1021/acsami.5b01452
ACS Appl. Mater. Interfaces 2015, 7, 11063–11068

demonstrate the short-range local structure. The Raman spectras are similar. There are five peaks at 191, 476, 513, 616, and 678 cm^{-1} in the Raman spectra of S1, S2, S3, and S4 at ambient conditions.[26,27] The band at 667 cm^{-1} is attributed to the characteristic of the octahedral sites (CoO_6), which is assigned to the A_{1g} species, in the O_{7h} spectroscopic symmetry. The Raman band located at 476 cm^{-1} has the E_g symmetry, whereas the band at 191, 513, 616 cm^{-1} corresponds to the tetrahedral sites (CoO_4), which is attributed to the F_{2g} symmetry. The oxidation states of Fe dopant was studied by XPS, and Figure S1c, d in the Supporting Information shows the Co 2p and Fe 2p XPS core levels for the S1 sample. Figure S1d in the Supporting Information shows the XPS spectra of Fe 2p doublet peaks; the binding energy of Fe 2p1/2 and Fe 2p3/2 was observed at approximately 723.9 and 710.4 eV, respectively. The splitting data between the Fe 2p1/2 and Fe 2p3/2 core levels are 13.5 eV, indicating a oxidation state of Fe^{3+} in the solid solution. Similarly, the core level spectra of Co 2p were curve fitted and are shown in Figure S1c in the Supporting Information. There are six multiplet peaks for Co 2p shown in the spectra. Peaks at 780.7 and 796.6 eV indicated Co^{2+} oxidation states, whereas peaks at 797.7 and 782.2 eV proved the presence of Co^{3+} oxidation states. Other peaks centered at 786.5 and 803.2 eV are satellite peaks.

The TEM images of solid solution S1 are shown in Figure 2 to furture illustrate the detailed microstructure. Figure 2a shows

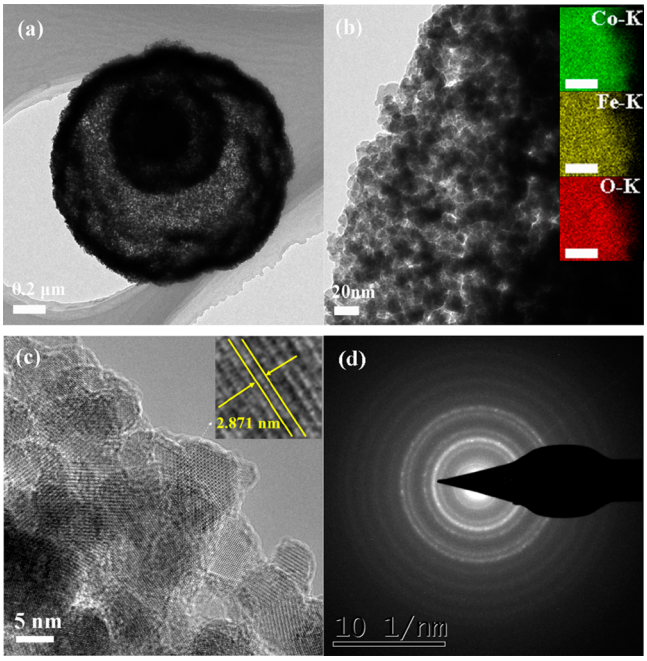

Figure 2. (a) TEM image of the S1, (b) high-magnification TEM image for S1 (inset, EDS mapping images, the scale bars correspond to 20 nm), (c) HRTEM image for S1, (d) SAED pattern of S1.

that the microsphere has the ball-in-ball hollow spherical characteristics with an inner core diameter of 750 nm. The enlarged view of the ball-in-ball structure indicates that the spheres are consist of small nanoparticles with a average size of around 10−20 nm (Figure 2c). The elemental mapping analysis of a part of the sphere confirmed the homogeneous distribution of Co, Fe, and O. The insets in Figure 2b correspond to the elements Co K-edge, Fe K-edge, and O K-edge, respectively. The HRTEM image in Figure 2c shows lattice spacings of 0.287 nm, corresponding to the (220) planes of S1. The selected-area electron diffraction (SAED) analysis (Figure 2d) further confirms the typical spinel structure of Co_3O_4. The detailed microstructure of S2, S3, and S4 is shown in the Supporting Informantion, Figure S3.

The nitrogen adsorption−desorption isotherms and pore size distribution curves by the Barrett−Joyner−Halenda (BJH) method of the solid solution are shown in the Supporting Informantion, Figure S4. The four nitrogen adsorption−desorption isotherms are similar to each others exhibiting characteristics of type I and type IV.[28] The specific surface areas of the soild solution S1, S2, S3, and S4 are 23.79, 56.4, 36.3, and 15 $m^2\ g^{-1}$, respectively. The hysteresis loop indicates the presence of mesopores. The Barret−Joyner−Halenda (BJH) results confirm the fact.

Figure 3a shows the cyclic voltammograms of the solid solution S1, S2, S3, and S4, respectively. There are two cathodic/anodic peaks at 0.90/1.59 V and 1.33/2.13 V for solid solution S1, S2, S3, and S4. The anodic/cathodic peaks of S1, S2, and S3 can be attributed to the redox reaction of Co ($3Co + 4Li_2O \rightleftarrows Co_3O_4 + 8Li^+ + 8e^-$)[29−32] and the Fe/$Fe^{3+}$ redox couples($2Fe + 3Li_2O \rightleftarrows Fe_2O_3 + 6Li^+ + 6e^-$).[33,34] However, the cathodic/anodic current peaks of S4 is due to Co ($3Co + 4Li_2O \rightleftarrows Co_3O_4 + 8Li^+ + 8e^-$).

The electrochemical performance of the solid solution S1 was also examined by the galvanostatic measurement. Figure 3b shows the first three cycles charge/discharge voltage profiles of the S1 electrode at a constant current density of 0.1 A g^{-1}. The long plateaus about 1 V in the discharging and those near 2 V in the charging are attributed to reduction of Co_3O_4 to Co and reformation of Co_3O_4 based on the mentioned conversion reaction consistenting with the CV results. The capacities of the first three cycles are 1227, 823, and 808 mA h g^{-1}. The extra capacity of the first discharge compared with thoeretical capacity(890 $mAhg^{-1}$) can be ascribed to the SEI layer formation on the surface of solid solution.[5,35] The first columbic efficiency is 65%. In the following cycles, the solid solution S1 shows good cycling stability and high stable reversible capacities.

The cycle performance of S1, S2, S3, and S4 at 1C are shown in Figure 3c. The initial discharge capacities at 1 A g^{-1} are 1103.3, 1065.6, 1543.8, and 981 mA h g^{-1}, respectively. The initial charge−discharge efficiency of S1, S2, S3, and S4 is 61.3%, 45.2%, 53%, and 45.6%. The capacities of the second cycle decrease. The electrolyte decomposition between electrode and electrolyte and the inevitable formation of solid electrolyte interphase (SEI) layer on the electrode surface may be the main reason for initial capacity loss. From the second cycle to 100th cycles, the capacities of S1, S2, S3, and S4 decrease. The S1 electrode shows a reversible capacity of 650.2 mA h g^{-1} with 91.6% retention. The capacities of S2 and S3 decrease from 631.4 and 702.5 to 595.2 and 549.8 mAh g^{-1}. The capacity of S4 have a sharp decrease from 631.4 mA h g^{-1} to 414.3 mA h g^{-1} with 65.6% retention. The above result shows that S1 gives the highest capacity. The charge−discharge efficiency of the samples The doping of Fe increase the capacities and the cycle stability of lithium battery.

In Figure 3d, the S1 cells were performed at different current density from 0.1 A g^{-1} to 10 A g^{-1} to examine the stability. The discharge capacities of S1 are 951.5, 854, 698.7, 586.3, 454.6, 303.9, and 201.6 mA h g^{-1} at the current densities of 0.1, 0.2, 0.5, 1, 2, 5, and 10 A g^{-1}, respectively. Even at a high current of 10 A g^{-1}, the S1 exhibited a high capacity of 201.6 mA h g^{-1}. In

DOI: 10.1021/acsami.5b01452
ACS Appl. Mater. Interfaces 2015, 7, 11063−11068

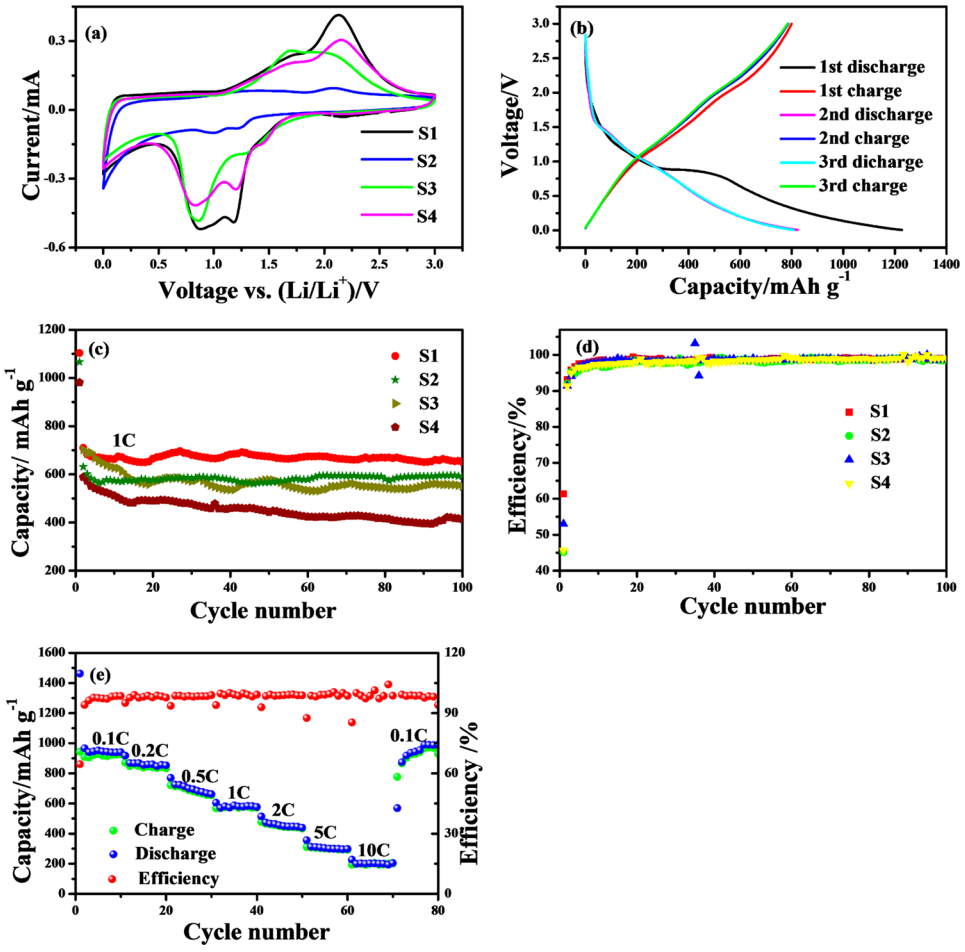

Figure 3. (a) Cyclic voltammogram of the solid solution $Co_xFe_{3-x}O_4$ at 0.2 mV s^{-1}, (b) first three charge/discharge curves of S1 at 0.1 A g^{-1}, (c) cycling performance for the solid-solution $Co_xFe_{3-x}O_4$ electrode discharging at 1Ag^{-1}, (d) efficiency or the solid-solution $Co_xFe_{3-x}O_4$ electrode discharging at 1 A g^{-1}, (e) rate performance of S1 for the discharging at variable rates from 0.1 to 10 A g^{-1}.

addition, the charge/discharge capacities can still be recovered to almost the same by using a small current density of 0.1 A g^{-1}. Doping alien cations and the hollow structure may be the reason for excellent rate performance. The doping is a efficient way to improve the electroconductivity and the porous structure can accommodate to the expansion in the Li^+ intercalation/deintercalation process. Figure 4 shows the TEM images of the S1 and S4 after 100 cycles. The microspheres slightly changed in the charge−discharge process, indicating the stability of the ball-in-ball structure.

The AC impedance were also carried out to gain insight into the superior electrochemical behavior of the solid solution S1, S2, S3, and S4 (Figure 5). The symbol R_Ω, R_{ct}, Z_w, C, and CPE in the equivalent circuit model represent the sum of all ohmic resistances from the electrode and the electrolyte, charge transfer resistance, Warburg impedance, intercalation capacity and the constant phase-angle element, respectively. Apparently, the charge-transfer resistance R_{ct} of S1, S2, S3 electrode are significantly smaller than that of S4, indicating that the doping lower the contact and charge-transfer impedances in the lithium ion insertion/extraction process and thus result in excellent rate performance.

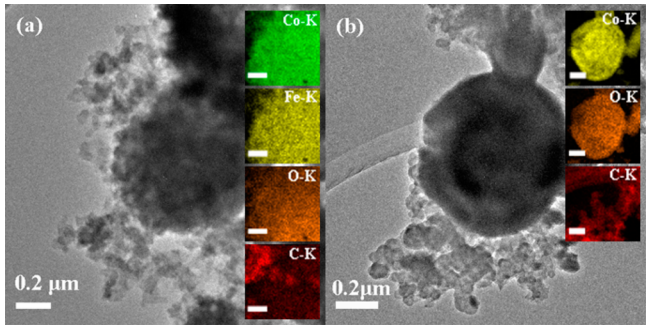

Figure 4. (a) TEM image of S1 (inset, EDS mapping images, the scale bars correspond to 200 nm) and (b) TEM image of S4 (inset, EDS mapping images, the scale bars correspond to 500 nm) after 100 cycles.

CONCLUSION

We have first prepared $Co_xFe_{3-x}O$ solid solution by a one-step hydrothermal method. Evaluated as electrode materials for lithium battery, the solid solution $Co_xFe_{3-x}O$ showed excellent cycle stability and rate performance. Cationic doping efficiently improved the electroconductivity and the ball-in-ball stucture significantly enhanced the material stability. Therefore, cationic doping is an efficient way to improve the electrochemical performance of transition metal oxides and potentially extended to other materials.

DOI: 10.1021/acsami.5b01452
ACS Appl. Mater. Interfaces 2015, 7, 11063−11068

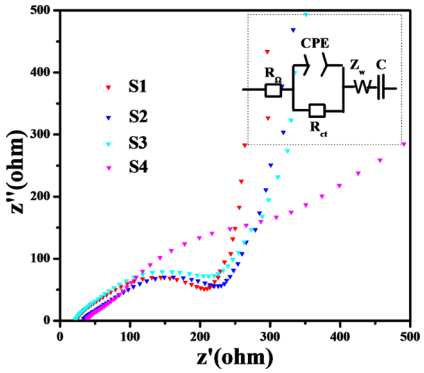

Figure 5. AC impedance of the solid solution $Co_xFe_{3-x}O_4$.

■ ASSOCIATED CONTENT

Supporting Information

Experimental details and additional characterization data, such as Raman and EDS, are shown in Figures S1–S5. The Supporting Information is available free of charge on the ACS Publications website at DOI: 10.1021/acsami.5b01452.

■ AUTHOR INFORMATION

Corresponding Author

*E-mail: wchengx@mail.sysu.edu.cn. Tel & Fax: +86-20-84113901.

Notes

The authors declare no competing financial interest.

■ ACKNOWLEDGMENTS

This work was financially supported by the National Natural Science Foundation of China (51125008, 11274392, U1401241).

■ REFERENCES

(1) Poizot, P.; Laruelle, S.; Grugeon, S.; Dupont, L.; Tarascon, J. M. Nano-Sized Transition-Metal Oxides as Negative-Electrode Materials for Lithium-Ion Batteries. *Nature* **2000**, *407*, 496–499.

(2) Ji, L.; Lin, Z.; Alcoutlabi, M.; Zhang, X. Recent Developments in Nanostructured Anode Materials for Rechargeable Lithium-Ion Batteries. *Energy Environ. Sci.* **2011**, *4*, 2682–2699.

(3) Malini, R.; Uma, U.; Sheela, T.; Ganesan, M.; Renganathan, N. G. Conversion Reactions: A New Pathway to Realise Energy in Lithium-Ion Battery—Review. *Ionics* **2008**, *15*, 301–307.

(4) Wu, R.; Qian, X.; Rui, X.; Liu, H.; Yadian, B.; Zhou, K.; Wei, J.; Yan, Q.; Feng, X.-Q.; Long, Y.; Wang, L.; Huang, Y. Zeolitic Imidazolate Framework 67-Derived High Symmetric Porous Co_3O_4 Hollow Dodecahedra with Highly Enhanced Lithium Storage Capability. *Small* **2014**, *10*, 1932–1938.

(5) Fei, L.; Lin, Q. L.; Yuan, B.; Naeemi, M.; Xu, Y.; Li, Y. L.; Deng, S. G.; Luo, H. M. Controlling Morphology and Enhancing Electrochemical Performance of Cobalt Oxide by Addition of Graphite. *Mater. Lett.* **2013**, *98*, 59–62.

(6) Wang, F.; Lu, C.; Qin, Y.; Liang, C.; Zhao, M.; Yang, S.; Sun, Z.; Song, X. Solid State Coalescence Growth and Electrochemical Performance of Plate-Like Co_3O_4 Mesocrystals as Anode Materials for Lithium-Ion Batteries. *J. Power Sources* **2013**, *235*, 67–73.

(7) Shen, L.; Song, H.; Cui, H.; Wen, X.; Wei, X.; Wang, C. Fe_3O_4-Carbon Nanocomposites Via a Simple Synthesis as Anode Materials for Rechargeable Lithium Ion Batteries. *CrystEngComm* **2013**, *15*, 9849–9854.

(8) Park, J.; Moon, W. G.; Kim, G.-P.; Nam, I.; Park, S.; Kim, Y.; Yi, J. Three-Dimensional Aligned Mesoporous Carbon Nanotubes Filled with Co_3O_4 Nanoparticles for Li-Ion Battery Anode Applications. *Electrochim. Acta* **2013**, *105*, 110–114.

(9) Bruce, P. G.; Scrosati, B.; Tarascon, J. M. Nanomaterials for Rechargeable Lithium Batteries. *Angew. Chem., Int. Ed.* **2008**, *47*, 2930–46.

(10) Shen, L.; Wang, C. Hierarchical Co_3O_4 Nanoparticles Embedded in a Carbon Matrix for Lithium-Ion Battery Anode Materials. *Electrochim. Acta* **2014**, *133*, 16–22.

(11) Jayaprakash, N.; Jones, W. D.; Moganty, S. S.; Archer, L. A. Composite Lithium Battery Anodes Based on Carbon@Co_3O_4 Nanostructures: Synthesis and Characterization. *J. Power Sources* **2012**, *200*, 53–58.

(12) Shenouda, A. Y.; Liu, H. K. Studies on Electrochemical Behaviour of Zinc-Doped Lifepo4 for Lithium Battery Positive Electrode. *J. Alloys Compd.* **2009**, *477*, 498–503.

(13) Wang, J.; Yang, J.; Xie, J.; Xu, N. A Novel Conductive Polymer–Sulfur Composite Cathode Material for Rechargeable Lithium Batteries. *Adv. Mater.* **2002**, *14*, 963–965.

(14) Wang, L.; Yu, Y.; Chen, P.-C.; Chen, C.-H. Electrospun Carbon–Cobalt Composite Nanofiber as an Anode Material for Lithium Ion Batteries. *Scripta Mater.* **2008**, *58*, 405–408.

(15) Yuan, T.; Yu, X.; Cai, R.; Zhou, Y.; Shao, Z. Synthesis of Pristine and Carbon-Coated $Li_4Ti_5O_{12}$ and Their Low-Temperature Electrochemical Performance. *J. Power Sources* **2010**, *195*, 4997–5004.

(16) Wang, L.; Yu, Y.; Chen, P. C.; Zhang, D. W.; Chen, C. H. Electrospinning Synthesis of C/Fe_3O_4 Composite Nanofibers and Their Application for High Performance Lithium-Ion Batteries. *J. Power Sources* **2008**, *183*, 717–723.

(17) Liu, H.; Cao, Q.; Fu, L. J.; Li, C.; Wu, Y. P.; Wu, H. Q. Doping Effects of Zinc on $LiFePO_4$ Cathode Material for Lithium Ion Batteries. *Electrochem. Commun.* **2006**, *8*, 1553–1557.

(18) Armand, M.; Tarascon, J. M. Building Better Batteries. *Nature* **2008**, *451*, 652–657.

(19) Shi, W.; Rui, X.; Zhu, J.; Yan, Q. Design of Nanostructured Hybrid Materials Based on Carbon and Metal Oxides for Li Ion Batteries. *J. Phys. Chem. C* **2012**, *116*, 26685–26693.

(20) Ogata, A.; Komaba, S.; Baddour-Hadjean, R.; Pereira-Ramos, J. P.; Kumagai, N. Doping Effects on Structure and Electrode Performance of K-Birnessite-Type Manganese Dioxides for Rechargeable Lithium Battery. *Electrochim. Acta* **2008**, *53*, 3084–3093.

(21) Yi, T.-F.; Xie, Y.; Jiang, L.-J.; Shu, J.; Yue, C.-B.; Zhou, A.-N.; Ye, M.-F. Advanced Electrochemical Properties of Mo-Doped $Li_4Ti_5O_{12}$ Anode Material for Power Lithium Ion Battery. *RSC Adv.* **2012**, *2*, 3541–3547.

(22) Wu, R.; Qian, X.; Zhou, K.; Wei, J.; Lou, J.; Ajayan, P. M. Porous Spinel $Zn_XCo_{3-X}O_4$ Hollow Polyhedra Templated for High-Rate Lithium-Ion Batteries. *ACS Nano* **2014**, *8*, 6297–6303.

(23) Matsumura, T.; Sonoyama, N.; Kanno, R.; Takano, M. Lithiation Mechanism of New Electrode Material for Lithium Ion Cells—the A-Fe_2O_3–SnO_2 Binary System. *Solid State Ionics* **2003**, *158*, 253–260.

(24) Xu, Y.; Dunwell, M.; Fei, L.; Fu, E.; Lin, Q.; Patterson, B.; Yuan, B.; Deng, S.; Andersen, P.; Luo, H.; Zou, G. Two-Dimensional V_2O_5 Sheet Network as Electrode for Lithium-Ion Batteries. *ACS Appl. Mater. Interfaces* **2014**, *6*, 20408–20413.

(25) Nytén, A.; Thomas, J. O. A Neutron Powder Diffraction Study of $LiCo_xFe_{1-x}PO_4$ for X=0, 0.25, 0.40, 0.60 and 0.75. *Solid State Ionics* **2006**, *177*, 1327–1330.

(26) Bouchard, M.; Gambardella, A. Raman Microscopy Study of Synthetic Cobalt Blue Spinels Used in the Field of Art. *J. Raman Spectrosc.* **2010**, *41*, 1477–1485.

(27) Tripathy, S. K.; Christy, M.; Park, N.-H.; Suh, E.-K.; Anand, S.; Yu, Y.-T. Hydrothermal Synthesis of Single-Crystalline Nanocubes of Co_3O_4. *Mater. Lett.* **2008**, *62*, 1006–1009.

(28) Ryu, Z.; Zheng, J.; Wang, M.; Zhang, B. Characterization of Pore Size Distributions on Carbonaceous Adsorbents by Dft. *Carbon* **1999**, *37*, 1257–1264.

(29) Cheng, F.; Tao, Z.; Liang, J.; Chen, J. Template-Directed Materials for Rechargeable Lithium-Ion Batteries. *Chem. Mater.* **2008**, *20*, 667–681.

DOI: 10.1021/acsami.5b01452
ACS Appl. Mater. Interfaces 2015, 7, 11063–11068

(30) Song, H.; Shen, L.; Wang, C. Template-Free Method Towards Quadrate Co_3O_4 Nanoboxes from Cobalt Coordination Polymer Nano-Solids for High Performance Lithium Ion Battery Anodes. *J. Mater. Chem. A* **2014**, *2*, 20597−20604.
(31) Fu, Y.; Li, X.; Sun, X.; Wang, X.; Liu, D.; He, D. Self-Supporting Co_3O_4 with Lemongrass-Like Morphology as a High-Performance Anode Material for Lithium Ion Batteries. *J. Mater. Chem.* **2012**, *22*, 17429−17431.
(32) Wang, L.; Liu, B.; Ran, S.; Huang, H.; Wang, X.; Liang, B.; Chen, D.; Shen, G. Nanorod-Assembled Co_3O_4 Hexapods with Enhanced Electrochemical Performance for Lithium-Ion Batteries. *J. Mater. Chem.* **2012**, *22*, 23541−23546.
(33) Li, Z.; Li, B.; Yin, L.; Qi, Y. Prussion Blue-Supported Annealing Chemical Reaction Route Synthesized Double-Shelled Fe_2O_3/Co_3O_4 Hollow Microcubes as Anode Materials for Lithium-Ion Battery. *ACS Appl. Mater. Interfaces* **2014**, *6*, 8098−8107.
(34) Yang, Z.; Shen, J.; Archer, L. A. An in Situ Method of Creating Metal Oxide−Carbon Composites and Their Application as Anode Materials for Lithium-Ion Batteries. *J. Mater. Chem.* **2011**, *21*, 11092.
(35) Wu, Z.-S.; Ren, W.; Wen, L.; Gao, L.; Zhao, J.; Chen, Z.; Zhou, G.; Li, F.; Cheng, H.-M. Graphene Anchored with Co_3O_4 Nanoparticles as Anode of Lithium Ion Batteries with Enhanced Reversible Capacity and Cyclic Performance. *ACS Nano* **2010**, *4*, 3187−3194.

DOI: 10.1021/acsami.5b01452
ACS Appl. Mater. Interfaces 2015, 7, 11063−11068